

# Adaptive fluid-structure interaction simulation of large-scale complex liquid containment with two-phase flow

Sung-Woo Park<sup>1</sup> and Jin-Rae Cho<sup>1,2\*</sup>

<sup>1</sup>School of Mechanical Engineering, Pusan National University, Busan 609-735, Korea

<sup>2</sup>Research and Development Institute of Midas IT, Gyeonggi 463-400, Korea

(Received March 2, 2011, Revised January 24, 2012, Accepted February 1, 2012)

**Abstract.** An adaptive modeling and simulation technique is introduced for the effective and reliable fluid-structure interaction analysis using MSC/Dytran for large-scale complex pressurized liquid containment. The proposed method is composed of a series of the global rigid sloshing analysis and the locally detailed fluid-structure analysis. The critical time at which the system exhibits the severe liquid sloshing response is sought through the former analysis, while the fluid-structure interaction in the local region of interest at the critical time is analyzed by the latter analysis. Differing from the global coarse model, the local fine model considers not only the complex geometry and flexibility of structure but the effect of internal pressure. The locally detailed FSI problem is solved in terms of multi-material volume fractions and the flow and pressure fields obtained by the global analysis at the critical time are specified as the initial conditions. An in-house program for mapping the global analysis results onto the fine-scale local FSI model is developed. The validity and effectiveness of the proposed method are verified through an illustrative numerical experiment.

**Keywords:** large-scale liquid containment; fluid-structure interaction; Adaptive FSI Simulation; Multi-material volume fractions; two-phase flow; coarse- and fine-scale models

---

## 1. Introduction

Large-scale complex liquid containments have been a troublesome obstacle for the monolithic fluid-structure interaction analysis (Morand and Ohayon 1995) because the integrated matrix equations become highly large-scale owing to a tremendous number of finite elements and control volumes. To resolve this inherent difficulty, several alternative numerical techniques were introduced by many investigators (Meckerle 1999). Two representative numerical techniques among them are the employment of a rigid tank sloshing model and the separate FSI analysis (Housner 1963, Rajasankar *et al.* 1993, Cho *et al.* 2001). In the former approach, the structure is excluded from the internal liquid sloshing analysis by neglecting the structure deformation. After that, the structure deformation due to the hydrodynamic pressure of liquid flow is calculated through the static structural analysis by specifying the critical hydrodynamic pressure on the structure boundary being

---

\*Corresponding author, Vice Director, E-mail: jrcho@pusan.ac.kr

in contact with liquid flow. Meanwhile, in the latter approach, the hydrodynamic pressure of liquid flow is reflected into the structural analysis by means of added mass which is calculated according to the virtual work principle (Cho and Song 2001). However, these alternative methods can not fully account for the coupling effect between the structural deformation and the fluid flow.

Currently, almost all the large-scale complex fluid-structure interaction problems are analyzed by the iterative staggered coupling approach (Piperno *et al.* 1995, Schäfer and Teschauer 2001, Sigrist and Abouri 2006). In this approach, the fluid flow and the structure deformation are basically solved separately and the coupling effects between the flow and the structure are reflected in the iterative staggered manner. The structure deformation alters the flow domain and boundary while the fluid flow imposes the hydrodynamic pressure on the structure boundary, and this indirect interaction job iterates up to the target time period of observation. Two representative coupling algorithms are widely used, an ALE coupling algorithm (Cho and Lee 2003) for the simple coupling surfaces and the Euler-Lagrange coupling algorithm for the complex coupling surfaces (Farhat *et al.* 1998). Regarding the time marching in the iterative staggered coupling process, Longatte *et al.* (2009) compared and discussed several partitioned fluid-structure code-coupling schemes in terms of stability and energy conservation properties. There is no doubt that the size of two separate matrices made by this approach is much smaller than an integrated matrix in the monolithic approach. Nevertheless, the increase of the total CPU time becomes still an inevitable difficulty as the fluid-structure interaction problem becomes large-scale and complex. In this context, a new concept of FSI analysis technique which can dramatically reduce the total CPU time is highly desirable.

The goal of this study is to introduce a CPU-time efficient iterative staggered coupled analysis using MSC/Dytran (2008) for large-scale complex fluid-structure interaction problems. This new concept of coupled analysis called the adaptive FSI modeling and simulation is motivated from the fact that the analyst's concern is neither for all the region of the FSI system nor at all the time. But, rather the severe local response at the critical time becomes the main concern. In this technique, both the critical region and time are sought by a coarse-scale global ideal flow analysis in which the structure is assumed to be rigid, while the detailed hydroelastic response of the local region of interest at the critical time is analyzed by the fine-scale local FSI analysis in which both the detailed flexible structure geometry and the mutual interaction between the structure and the flow are fully considered. Both the global and local analyses are carried out by MSC/Dytran, while the mapping of the global analysis results onto the fine-scale local model is performed by our in-house program. The validity and the CPU-time efficiency are illustrated through the numerical experiment of the insulation containment of LNG carrier.

## 2. Problem description

### 2.1 Large-scale complex fluid-structure interaction problems

Large-scale complex fluid-structure interaction systems can be found in a variety of engineering and science fields, and two representative examples are shown in Fig. 1. Referring to Fig. 1(a), natural gas (NG) is conveyed from the place of origin to each consuming country by LNG carrier, as a state of extremely low-temperature liquefied natural gas (LNG) filled within the specially designed cargos called the insulation containments. The wave-induced ship motion causes the large

amplitude free-surface fluctuation of interior LNG so that the insulation containment should be designed to sufficiently resist the resulting hydrodynamic impact load (Kyoung *et al.* 2005). However, the insulation containment is in the highly complex lamination structure, as will be shown later, so that the hydroelastic simulation considering both the detailed lamination structure and the fluid-structure interaction effect is not available by the conventional analysis technique. Meanwhile, the hydroplaning analysis shown in Fig. 1(b) of patterned tire requires over the total of 80,000 finite elements and control volumes to generate a 3-D coupled FEM and FVM model (Cho *et al.* 2006), and furthermore the total CPU time spent for a revolution of the tire model on Pentium IV PC reaches a week.

Owing to this limitation, traditionally the fluid-structure interaction simulation has been carried out either by simplifying the complex structure geometry or by completely excluding the structural deformation. An illustrative example is a rigid tank sloshing model for the LNG-containment interaction problem as shown in Fig. 2(a), where the complex containment lamination shown in Fig. 2(b) is assumed to be completely rigid. In this simplest model, not only the fluid-structure interaction but the cushioning effect of NG above the LNG free surface could not be taken into consideration. As mentioned earlier, the structural strength against the hydrodynamic impact has been evaluated through the static structural analysis by imposing the hydrodynamic pressure on to the insulation containment.

The interior fluid flow has been generally assumed to be inviscid so that the fluid flow has been

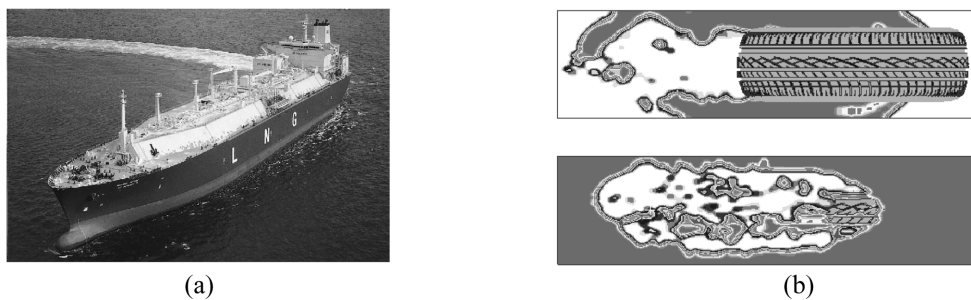


Fig. 1 Illustration: (a) hydroelastic impact caused by interior LNG sloshing; and (b) hydroplaning of patterned tire

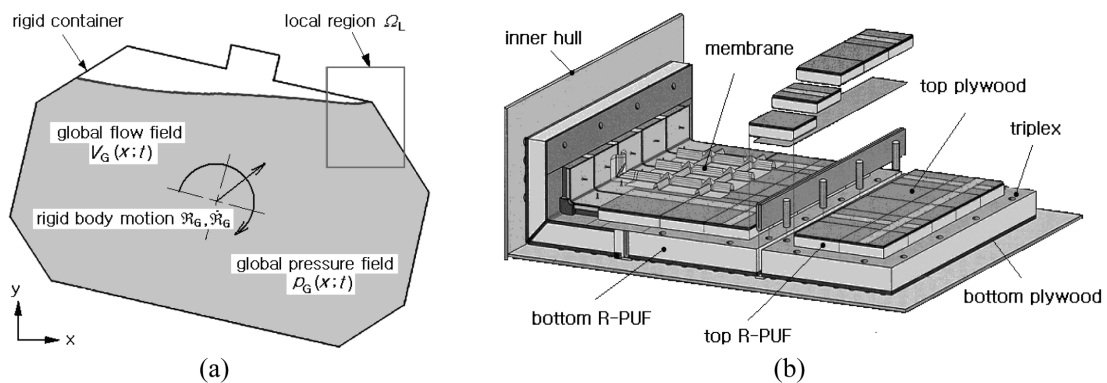


Fig. 2 LNG containment: (a) rigid tank sloshing model; and (b) lamination structure

formulated in terms of the ideal flow velocity or the velocity potential. Denoting  $\Omega_F \in \mathbb{R}^3$  be the time-varying flow domain with the moving boundary  $\partial\Omega_F^S$ , the ideal flow velocity  $\mathbf{V}(\mathbf{x};t)$  in the Eulerian kinematic description is governed by the conservation of mass

$$\frac{\partial \rho_F}{\partial t} + \rho_F(\nabla \cdot \mathbf{V}) = 0, \quad \text{in } \Omega_F \times (0, T] \tag{1}$$

and the momentum equations

$$\rho_F \frac{\partial \mathbf{V}}{\partial t} + \rho_F(\mathbf{V} \cdot \nabla)\mathbf{V} = \nabla \cdot \boldsymbol{\sigma}^F, \quad \text{in } \Omega_F \times (0, T] \tag{2}$$

and the transport equation

$$\frac{\partial F}{\partial t} \times \mathbf{V} \cdot \nabla F = 0, \quad \text{in } \Omega_F \times (0, T] \tag{3}$$

subject to the associated initial and boundary conditions. Here,  $\rho_F$  is the flow density and  $\boldsymbol{\sigma}^F$  is the flow-induced stress tensor:  $\boldsymbol{\sigma}^F = -p\mathbf{1}$  with  $p$  being the hydrodynamic pressure and  $\mathbf{1}$  being the unit tensor. In addition,  $F(\mathbf{x};t) \in [0, 1]$  denotes the volume fraction of liquid which is required to identify the free surface of flow. It should be noted that pressure in the upper region above LNG is set by zero by excluding NG filled in this region from the rigid tank sloshing model.

### 2.2 The motivation and concept

Fluid-structure interaction analyses provide the time histories of the associated quantities of interest, but in most cases the analyst’s concern focuses on several local regions showing the relatively high responses. It implies that the significance of the time response is not same for the entire problem domain and during all the time period of observation, which is the underlying motivation behind the adaptive FSI modeling and simulation. It should be note that both the local region and the critical time exhibiting the peak responses, of course, are not known *a priori*, so that both should be determined before the local response at the critical time is analyzed in details.

The concept of the state-of-the-art fluid-structure interaction modeling and simulation is schematically represented in Fig. 3, by taking the large-scale complex LNG insulation containment

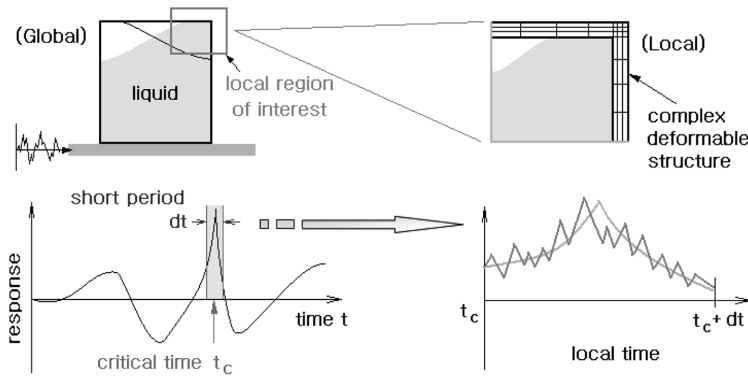


Fig. 3 Schematic representation of the adaptive FSI modeling and simulation

as an example. The critical location and time in the hydroelastic response of the containment are searched through the local analysis using the coarse-scale rigid tank sloshing model, under the physical fact that the peak hydrodynamic pressure gives rise to the highest impact to the insulation containment. Once the local region of interest and the critical time are determined, the local fine-scale fluid-structure interaction simulation is performed during a short time period. In the fine-scale FSI model, both the detailed geometry and flexibility of the containment and the interaction effect between the fluid flow and the structure deformation are fully considered.

The numerical responses obtained by the coarse-scale global analysis at the critical time are used as the initial and boundary conditions for the local analysis (Mao and Sun 1991), and the transfer of the global values to the fine local region is made by the linear interpolation in our in-house program. It should be noted that the fluid flow in the local problem deviates from one in the global problem as the time period of observation increases, because the local fluid flow is governed by the initial and boundary values which are mapped from the global analysis results at the critical time.

### 3. Adaptive FSI modeling and simulation

#### 3.1 Fine-scale local FSI model

Referring to Fig. 2(a), let us assume that the right upper corner of the insulation containment exhibits the critical hydroelastic response such that the fine-scale local FSI analysis is required. As mentioned earlier, both the critical region and time are found from the coarse-scale global analysis. A fine-scale FSI problem for such a local region  $\Omega_L \in \mathcal{R}^3$  at the critical time  $t^c$  is schematically represented in Fig. 3(a) where not only the LNG flow but the detailed containment geometry and the upper NG flow are taken into consideration. Differing from the global sloshing problem described in Section 2.1, the fine-scale local problem is characterized by the interaction between the internal two-phase flow and the flexible containment deformation. Two subscripts  $G$  and  $L$  and two superscripts  $f$  and  $g$  stand for global, local, LNG and NG respectively, and the remaining geometry and physical quantities shown in Fig. 3(a) will be defined in Section 3.3. Note that NG which is mostly composed of  $C_2H_4$  is produced according to the vaporization of LNG caused by the external heat invasion into the insulation containment during the laden voyage. The detailed local flexible insulation containment is inserted into the rigid tank such that its bottom surface being in contact with the internal flow coincides with the rigid tank surface.

Referring to Fig. 4(b), the fine-scale FEM mesh of the local flexible containment is assembled into a rigid shell dummy enclosure, because the resulting outer surface of the local containment should be a convex enclosure such that the general Euler-Lagrange coupling algorithm of MSC/Dytran could be applied. The dimension and the more detailed configuration of the local containment FEM mesh will be represented in Fig. 9(a) in Section 4. The rigid shell dummy and the local flexible containment are assembled using the node-to-node tying between the containment lower surface and dummy membrane surface and using a number of massless rigid elements between the inner/outer hulls and the rigid dummy. The rigid body motion of the rigid tank which is specified for the global analysis will be specified to this rigid dummy-containment assembly in the fine-scale local FSI analysis.

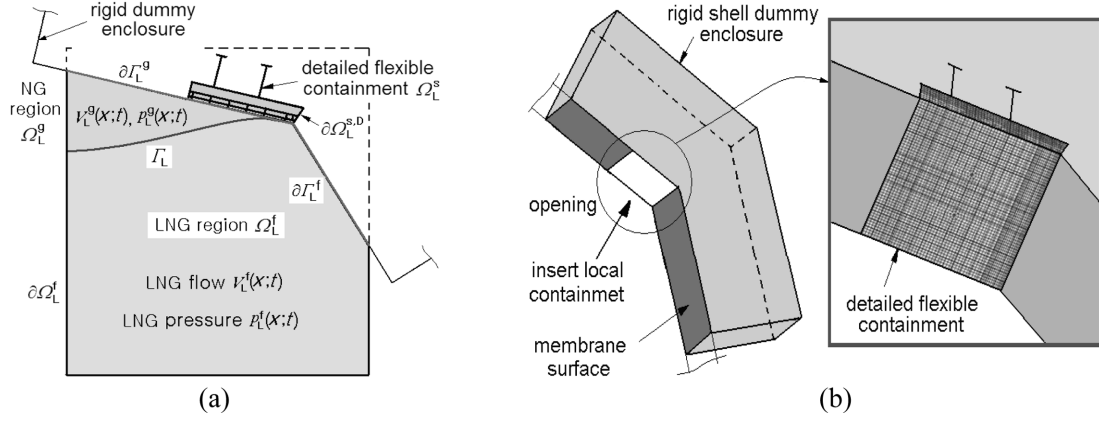


Fig. 4 Fine-scale local FSI model: (a) domain definition, (b) rigid dummy-containment assembly

### 3.2 Fine-scale local FSI problem with internal two-phase flow

Referring to Fig. 4(a), the fine-scale FSI domain  $\Omega_L \in \mathfrak{R}^3$  is composed of the Euler region  $\Omega_L^E \in \mathfrak{R}^3$  and the rigid dummy-containment assembly  $\Omega_L^S \in \mathfrak{R}^3$ . The total Euler region  $\Omega_L^E \in \mathfrak{R}^3$  and the common interface  $\Gamma_L$  between LNG and NG in the fine-scale FSI domain  $\Omega_L \in \mathfrak{R}^3$  are defined by  $\Omega_L^E = \Omega_L^f \cup \Omega_L^g$  and  $\Gamma_L = \Omega_L^f \cup \Omega_L^g$ . In addition, NG filled in the upper region is assumed to be ideal gas obeying the  $\gamma$ -law gas equation (Barler *et al.* 2008) given by

$$p^g = (1 - \gamma)\rho^g e^g \quad (4)$$

with  $\gamma = 1$ ,  $\rho^g$  and  $e^g$  being the density and the internal energy of NG.

Then, the local flow velocity fields  $\mathbf{V}_L^I (I=f, g)$  of each media in the local Euler region, during the short time period  $T^\tau \in [t^c, t^c + \varepsilon]$  are governed by the conservation laws of mass

$$\frac{\partial \rho^I}{\partial \tau} + \rho^I (\nabla \cdot \mathbf{V}_L^I) = 0, \quad \text{in } \Omega_L^I \times (0, T^\tau], \quad I = f, g \quad (5)$$

and the momentum equations

$$\rho^I \frac{\partial \mathbf{V}_L^I}{\partial \tau} + \rho^I (\mathbf{V}_L^I \cdot \nabla) \mathbf{V}_L^I = \nabla \cdot \boldsymbol{\sigma}_L^I, \quad \text{in } \Omega_L^I \times (0, T^\tau], \quad I = f, g \quad (6)$$

with the initial conditions

$$\mathbf{V}_L^f(\mathbf{x}; 0) = \mathbf{V}_G^f(\mathbf{x}; t^c), \quad p_L^f(\mathbf{x}; 0) = p_G^f(\mathbf{x}; t^c) \quad \text{for LNG} \quad (7)$$

$$\mathbf{V}_L^g(\mathbf{x}; 0) = 0, \quad p_L^g(\mathbf{x}; 0) = p^g \quad \text{for NG} \quad (8)$$

and the boundary conditions

$$\mathbf{V}_L^I(\mathbf{x}; \tau) \cdot \mathbf{n}_L^I = \frac{\partial \tilde{\mathbf{u}}^I}{\partial \tau} \cdot \mathbf{n}_L^I \quad \partial \Gamma_L^I \times (0, T^\tau), \quad I = f, g \quad (9)$$

Where,  $\mathbf{n}_L^f$  and  $\mathbf{n}_L^g$  are the outward unit vectors normal to the LNG and NG boundaries and  $\tilde{\mathbf{u}}^L$  denotes the displacement of the rigid dummy-containment assembly shown in Fig. 4(b). In addition,  $\partial\Gamma_L^I$  denotes the interface between the structure and the internal two-phase flow.

Meanwhile, the volume fractions  $F(\mathbf{x};t)_L \in [0, 1]$  are introduced to identify the LNG and NG regions which are calculated using the following transport equations

$$\frac{\partial F_L^I}{\partial \tau} + \mathbf{V}_L^I \cdot \nabla F_L^I = 0, \quad \text{in } \Omega_L^I \times (0, T^\tau), \quad I = f, g \quad (10)$$

$$F_L^f(\mathbf{x};0) = F_G(\mathbf{x};t^c) \geq F^c \quad \text{in } \Omega_L^f, \quad F_L^g(\mathbf{x};0) = F_G(\mathbf{x};t^c) < F^c \quad \text{in } \Omega_L^g \quad (11)$$

Here,  $F^c$  indicates the cut-off volume fraction for setting the initial interface  $\Gamma_L$  between LNG and NG for the fine-scale local FSI problem with two-phase flows. As shown in Fig. 2(a), the global rigid tank sloshing problem is single LNG material flow so that only the LNG volume fraction is defined.

On the other hand, the undamped displacement field  $\mathbf{u}^L$  of the local flexible containment  $\Omega_L^s$  with boundary  $\partial\Omega^L = \partial\Omega_L^{s,D} \cup \partial\Gamma_L^I$  is governed by

$$\sigma_{ij}^L(\mathbf{u}^L)_{,j} + \rho^s(f_i - \ddot{u}_i^L) = 0, \quad \text{in } \Omega_L^s \times (0, T^\tau) \quad (12)$$

with the initial conditions

$$\mathbf{u}^L(\mathbf{x};0) = \mathfrak{R}_G(\mathbf{x};t^c), \quad \dot{\mathbf{u}}^L(\mathbf{x};0) = \dot{\mathfrak{R}}_G(\mathbf{x};t^c) \quad (13)$$

and the boundary conditions

$$\mathbf{u}^L(\mathbf{x};\tau) = \hat{\mathbf{u}}^L(\mathbf{x};\tau), \quad \text{on } \partial\Omega_L^{s,D} \times (0, T^\tau) \quad (14)$$

$$\sigma_{ij}^L(\mathbf{x};\tau)n_j^s n_i^s = -p_L^I(\mathbf{x};\tau), \quad \text{on } \partial\Gamma_L^I \times (0, T^\tau), \quad I = f, g \quad (15)$$

Here,  $\mathfrak{R}_G(\mathbf{x};t^c)$  and  $\dot{\mathfrak{R}}_G(\mathbf{x};t^c)$  are the rigid body displacement and velocity of the insulation containment at the critical time  $t^c$ . Furthermore,  $\partial\Omega_L^{s,D}$  and  $\hat{\mathbf{u}}^L(\mathbf{x};\tau)$  denote the Dirichlet boundary region and the displacement constraint by the rigid dummy enclosure which moves along with the rigid body motion of the insulation containment.

The fluid-structure interaction is implemented by the Euler-Lagrange coupling algorithm in the iterative staggered manner. The reader may refer to (Sigrist and Abouri 2006, Cho *et al.* 2006, Aquelet *et al.* 2006, Longatte *et al.* 2009) for more details on the partitioned fluid-structure coupling.

#### 4. Numerical experiments

We consider an insulation containment with the length  $L = 42.84$  m, the width  $B = 37.4$  m and the height  $H = 27.2$  m, in which the lower and upper regions are filled up with LNG and NG respectively. Remind that NG filled in the upper region is not considered in the global rigid tank sloshing problem, as mentioned earlier. The material properties of these two media are given in

Table 1 Material properties of LNG and NG

Material	Properties	Values
LNG	Filling ratio of LNG $\eta_R$ (%)	95
	Density $\rho^f$ (kg/m <sup>3</sup> )	500
	Bulk modulus $K$ (GPa)	1.44
NG	Density $\rho^g$ (kg/m <sup>3</sup> )	0.7136
	Specific internal energy $e^g$ (J/kg)	$5.858 \times 10^5$
	Cut-off volume fraction $F^c$	0.33

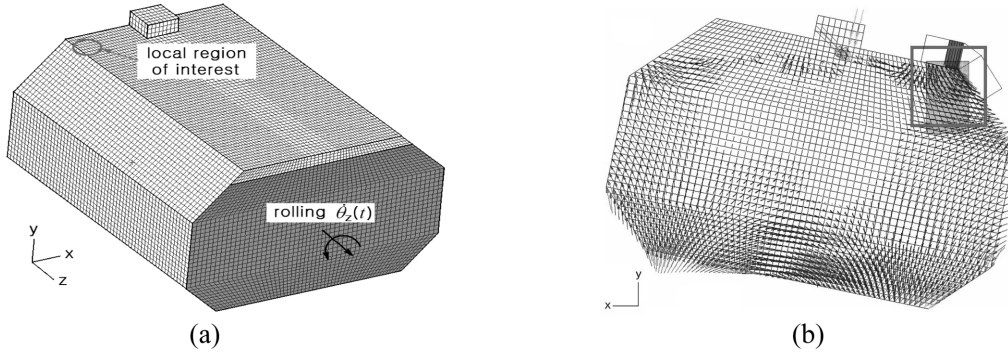


Fig. 5 (a) Finite element model of rigid tank; and (b) flow velocity field at the critical time

Table 1, where the cut-off volume fraction  $F^c$  indicates the critical volume fraction of LNG at the critical time in the rigid tank sloshing simulation. Based upon this critical volume fraction, LNG and NG regions within the local Euler region  $\Omega_L^E$  are distinguished and identified in the local FSI simulation. As given in Eq. (11), the Euler region with  $F_G < F^c$  is treated as NG while the remaining Euler region with  $F_G \geq F^c$  becomes LNG.

The interior Eulerian region and the rigid container are uniformly discretized with 135,608 control volume elements and 48,366 rigid shell elements. The numerical simulation is carried out with the commercial MSC/Dytran (2008), and the interfacing between the LNG flow and the rigid container is implemented by the ALE coupling algorithm of MSC/Dytran because the geometry of the rigid tank-LNG interface is simple and regular. The insulation containment is subjected to the sinusoidal rolling excitation shown with respect to the rolling axis, as shown in Fig. 5(a). The angular velocity is set as  $\dot{\theta}_z(t) = a\omega\cos(\omega t)$  with the amplitude  $a = 3.87^\circ$  and the angular frequency  $\omega = 2\pi/5.5$  (rad/sec), based upon the actual measurement data in the shipping service.

The time period  $T$  of observation was set by 4,014 sec for the rigid-tank sloshing simulation from the fact that the critical situations have empirically occurred at the time around 4,000 sec. The time incremental simulation was terminated in 1,115,508 iterations with averaged time step size  $\Delta\bar{t} = 3.598 \times 10^{-3}$  sec. Fig. 5(b) shows the sloshing flow velocity field of interior LNG at time 4,002 sec when the rigid containment rolls down by  $12^\circ$  counter-clockwise. The critical time was chosen from the fact that the upper corner indicated by circle is subjected to the remarkable hydrodynamic pressure at the critical time when LNG is flowing up along the containment inner surface at the upper corner. It has been found from the detailed numerical results that the peak flow

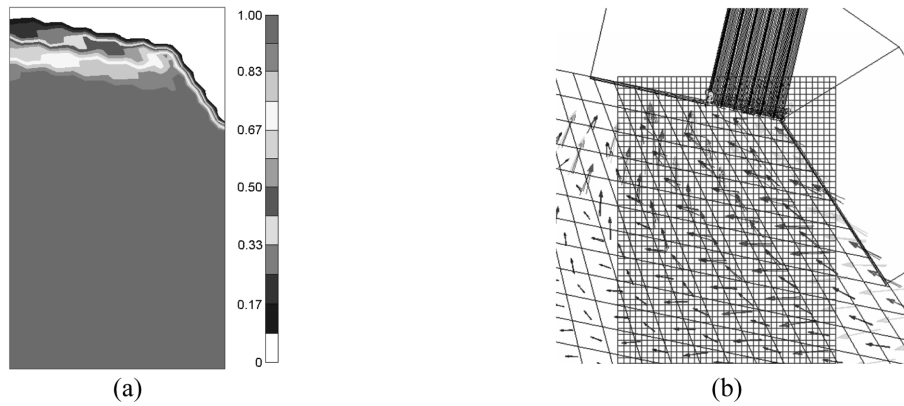


Fig. 6 In the local upper corner region: (a) volume fraction of LNG at the critical time; and (b) mapping between coarse and fine grids

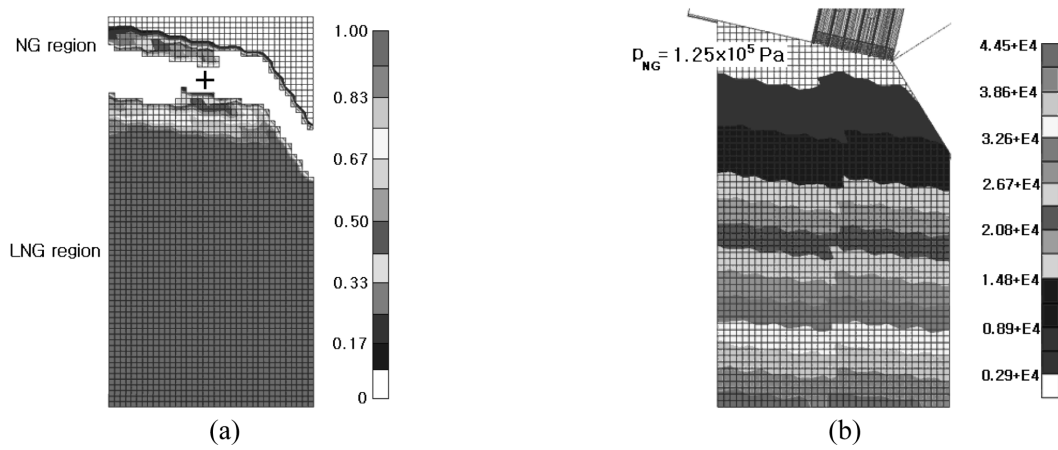


Fig. 7 Initial setting for the local Euler region: (a) LNG and NG regions; and (b) pressure fields

velocity and the peak hydrodynamic pressure in the upper local region at the critical time are 1.26 m/sec and 0.142 MPa, respectively.

Fig. 6(a) shows the distribution of LNG volume fraction  $F_G$  within the upper corner region at the critical time. The volume fraction, the velocity field  $\mathbf{V}_G$  and the pressure field  $p_G$  obtained by the coarse-scale global analysis at the critical time is used as the initial values for the fine-scale local FSI analysis. Fig. 6(b) overlaps the coarse-scale rigid tank model and the fine-scale local FSI model. The fine-scale Euler grid is generated with the total of 31,598 uniform control volumes, and the above-mentioned three global values are mapped into the fine grid by the linear interpolation. Note that three global values in the void region above the LNG free surface are set zero at this mapping stage. The mapping of the global values on the fine-scale local FSI model is performed by our in-house program.

In the next step, the fine-scale local Euler region  $\Omega_L^E$  is divided into LNG and NG regions by judging whether the mapped LNG volume fraction  $F_G$  is greater than the cut-off volume fraction  $F^c = 0.33$  or not, as represented in Fig. 7(a). For the NG region  $\Omega_L^g$ , the NG density  $\rho^g$  given in

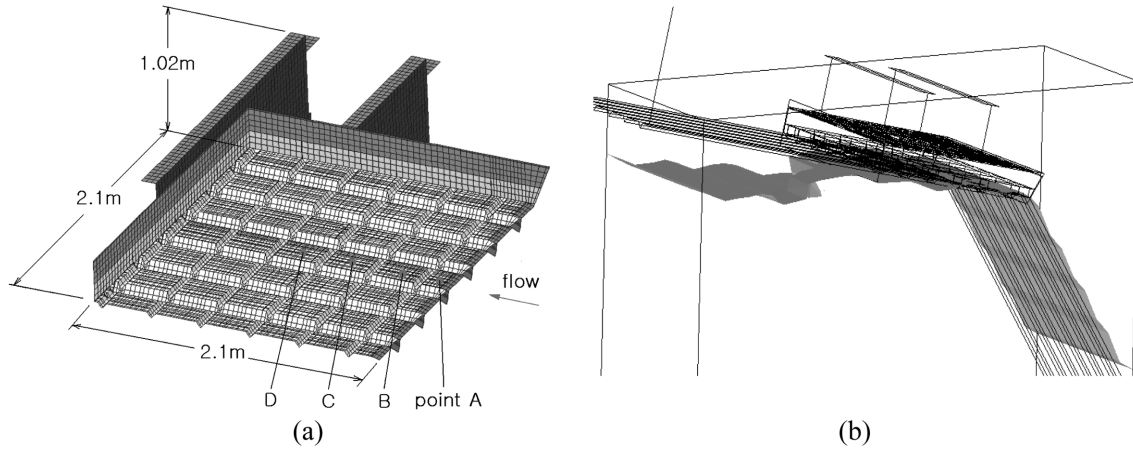


Fig. 8 (a) Finite element model of the local flexible insulation containment; and (b) LNG-NG interface at time 50 ms

Table 2 Material and mesh data for numerical experiments (isotropic components)

Items	Insulation components				
	Membrane	Plywood	Triplex	Mastics	Hull
Density $\rho^s$ (kg/m <sup>3</sup> )	7,850	710	2,500	2,500	7,850
Young's modulus $E$ (GPa)	200	8.2	13.13	2.87	206
Poisson's ratio $\nu$	0.27	0.17	0.3	0.3	0.3
Thickness $t$ (mm)	1.2	9 (top) 12 (bottom)	6	10	18
Number of elements	5,806	4,620 (top) 5,843 (bottom)	5,082	1,081	8,547
Element type		4-node shell		8-node solid	4-node shell

Table 1 with the zero initial velocity and the uniform gas pressure of NG  $p_{NG}$  of  $1.25 \times 10^5$  Pa which is calculated using the  $\gamma$ -law gas Eq. (4) is specified, as represented in Fig. 7(b). During the fine-scale local FSI analysis, the common interface  $\Gamma_L$  between LNG and NG is identified by curve-fitting the grid points of the control volumes having the cut-off volume fraction.

The dimension and the detailed geometry of the local flexible containment  $\Omega_L^s$  are shown in Fig. 8(a), and its finite element mesh is constructed with the total of 83,911 elements. The material properties, the element types and the element numbers for each insulation layer are recorded in Tables 2 and 3. The total element number is chosen such that the stress concentration occurred at each insulation layer can be captured with the reasonable accuracy. The top and bottom R-PUFs are modeled as orthotropic materials with the material properties given in Table 3, where the material co-ordinate 3 coincides with the thickness direction of the insulation containment. The contact condition is specified to the interface between membrane and top plywood, while the remaining interfaces between the insulation layers are completely bonded. Referring to Fig. 4(b), the closed outer surface of the dummy-containment assembly is defined as a coupling surface. The rigid dummy-containment assembly is modeled with the total of 104,649 finite elements in which the

Table 3 Material and mesh data for orthotropic R-PUFs

Items	Values
Density $\rho^s$ (kg/m <sup>3</sup> )	125
Young's moduli $E_1, E_2, E_3$ (MPa)	131, 131, 50
Shear moduli $G_{12}, G_{23}, G_{13}$ (MPa)	12.2, 12.2, 12.2
Poisson's ratios $\nu_{12}, \nu_{23}, \nu_{13}$	0.2, 0.153, 0.153
Thickness $t$ (mm)	120 (top), 150 (bottom)
Number of elements	15,246 (top), 5,843 (bottom) – 8-node solid

coupling surface is discretized with 7,466 4-node rigid shell elements for the rigid dummy and 5,806 4-node flexible shell elements for membrane.

Meanwhile, the dummy-containment assembly is forced to rotate with the containment centroid in the center with the angular velocity at time  $\theta_z(\tau) = a\omega\cos(\omega(t^c + \tau))$ . Its initial position can be determined from the rotation angle of the global rigid containment at the critical time  $t^c$ . The time period  $T^r$  of observation for the fine-scale local FSI analysis by MSC/Dytran was set by 50 m sec and the simulation was terminated in 53,342 iterations with the averaged time step size  $\Delta\bar{\tau} = 9.370 \times 10^{-7}$  sec. Differing from the global analysis, the Euler-Lagrange coupling algorithm of MSC/Dytran is used because of the complex membrane geometry. The NG-LNG interface free surface at the local time  $\tau$  of 50 ms is illustrated in Fig. 8(b), where the local LNG flows up along the corrugated membrane surface in the direction shown in Fig. 8(a). Hydrodynamic pressure caused by the two-phase flow is measured at four different points on the membrane surfaces which are positioned in consecutive order in the flow direction.

Fig. 9(a) shows the time-histories of hydrodynamic pressures of LNG at four different points on the membrane surface when NG is considered, where the horizontal axis indicates the lapse of time from the critical time  $t^c$ . One can clearly observe the delay in the initial hydrodynamic impact due to the evaluation point and that the peak hydrodynamic pressure occurs at point B. And, it is

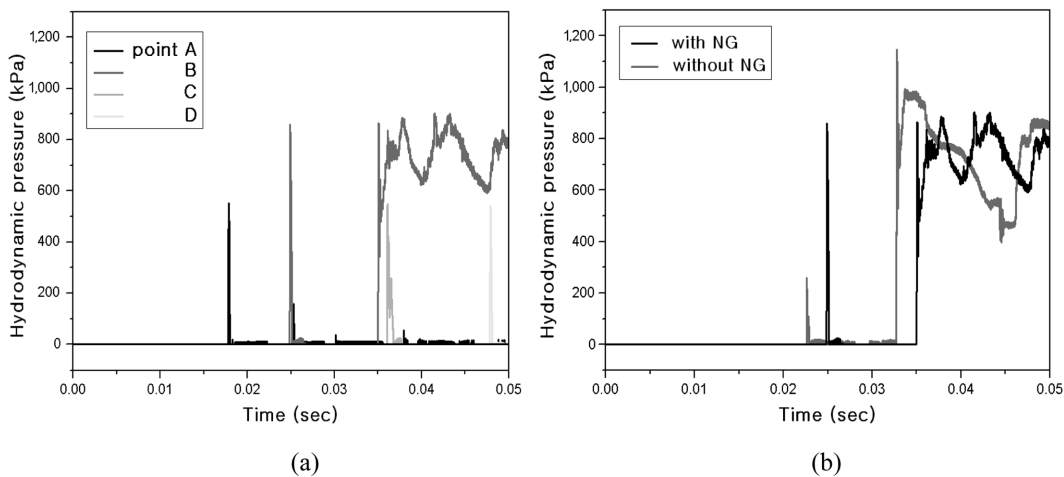


Fig. 9 Time histories of the hydrodynamic pressure of LNG acting on membrane: (a) at four points; and (b) comparison between with and without NG (at point B)

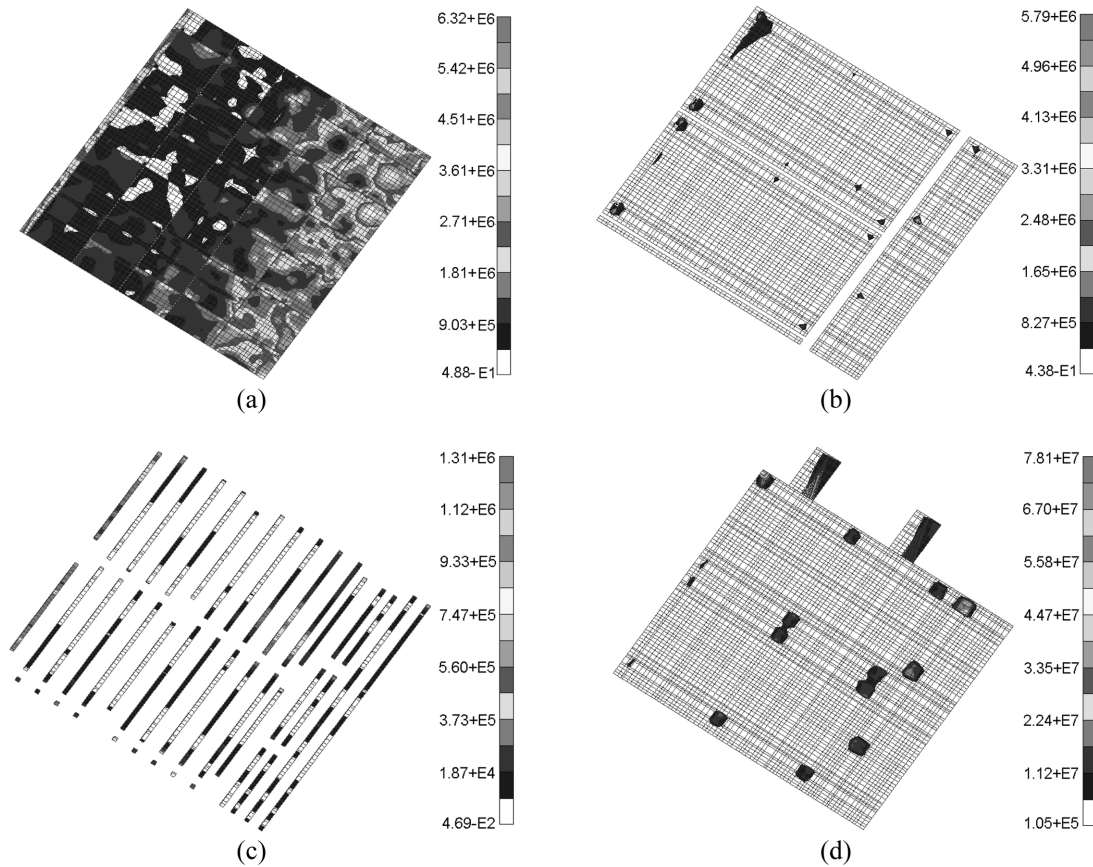


Fig. 10 Effective stress distributions at 34 ms: (a) top plywood; (b) bottom plywood; (c) mastics; and (d) hull

observed that three points A, C and D show only the apparent initial pressure impulses, differing from point B showing not only the initial pressure impulse but the subsequent continuous oscillating hydrodynamic pressure. The comparison of the hydrodynamic pressure time histories at point B between single- and two-phase sloshing flows is represented in Fig. 9(b), both the apparent reduction of the peak hydrodynamic pressure and the remarkable delay in the initial hydrodynamic impact are observed. It has been found from the detailed numerical results that the peak hydrodynamic pressure is reduced by 21.43% and the initial impact time is delayed by 2.22 ms respectively. It is because the cushioning effect (Xia *et al.* 2009) of the NG flow between the membrane and the lower LNG flow prevent the direct hydrodynamic impact of the LNG sloshing flow onto the membrane surface.

The effective stress distributions within four major components in the insulation containment at the local time  $\tau$  of 34 ms are represented in Fig. 10. The locations of each component can be referred to the previous Fig. 2(b) and the structural safety of these four components is known to be strongly influenced by the hydrodynamic impact. These detailed stress distributions of each structural component within the large-scale complex insulation containment illustrate a prominent ability of the proposed adaptive FSI modeling and simulation technique, because these detailed numerical results are not possible by the conventional non-adaptive FSI simulation method. It is

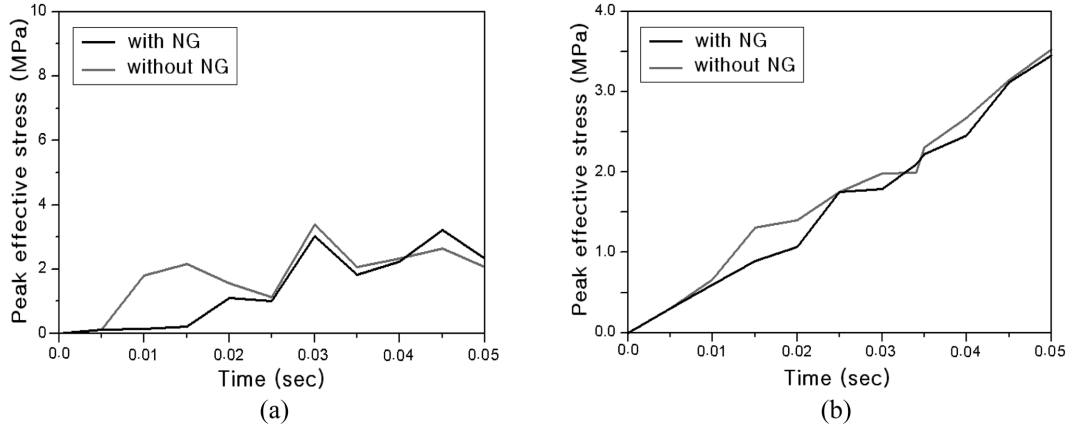


Fig. 11 Time histories of the peak effective stress: (a) top plywood; and (b) bottom plywood

Table 4 Comparison of the peak effective stresses between the fine models without and with NG

Cases	Peak effective stresses (MPa)						
	Top plywood	Top R-PUF	Triplex	Bottom R-PUF	Bottom plywood	Mastics	Hull
Without NG	3.38	$380 \times 10^{-3}$	$227 \times 10^{-3}$	$144 \times 10^{-3}$	3.52	1.02	81.3
With NG	3.04 (-10.1%)	$383 \times 10^{-3}$ (0.8%)	$207 \times 10^{-3}$ (-8.8%)	$148 \times 10^{-3}$ (2.8%)	3.45 (-2.0%)	1.04 (2.0%)	80.7 (-0.7%)

(\*): relative differences with respect to those obtained without NG

found from the comparison of four stress distributions that the stress level of hull is much higher than the remaining three components.

Time-histories of the peak effective stresses at the top and bottom plywoods are represented in Figs. 11(a) and 10(b) respectively, where the stress level reduction due to the cushioning effect of NG is clearly observed. Differing from the hydrodynamic pressure acting on the membrane surface, the noticeable delay in the time-histories is not observed. It is because the stress at each structural component within the insulation containment is caused not only by the hydrodynamic pressure of LNG acting on the membrane but by the internal pressure of NG. Top plywood shows the stress time-history similar to one of hydrodynamic pressure acting on the membrane, but bottom plywood does almost linear increase with the lapse of time owing to the time delay in transferring the hydrodynamic impact on the membrane surface to bottom plywood. The peak effective stresses occurred at all the insulation components when the fine-scale local FSI simulation was done with and without considering NG are compared in Table 4. Top plywood and triplex show the apparent significant reduction in the peak effective stresses, while the effect of NG on the peak effective stresses at the remaining components is not shown to be remarkable within the range of the numerical time integration accuracy.

One can infer the advantage of the proposed adaptive technique from Table 5 where several important simulation data required for both the coarse-scale global and fine-scale local analyses. Contrary to the coarse-scale global analysis requiring the total CPU time of 20 hrs for the

Table 5 Comparison of the simulation data required for each analysis

Items	Coarse-scale global analysis	Fine-scale local analysis
Total number of elements	183,974	136,247
Time period of observation (sec)	4,014	0.05
Averaged time step size $\Delta t$ (sec)	$3.598 \times 10^{-3}$	$9.370 \times 10^{-7}$
Total number of iterations	1,115,508	53,342
Total CPU time (hr)	19.73	10.85

simulation up to 4,014 sec, the fine-scale local analysis requires over 10 hrs to simulate only the hydrodynamic response of the local flexible containment during 50 m sec. Thus, there is no doubt that the hydroelastic analysis up to 4,014 sec, using the fine-scale global containment model in which each insulation components are modeled in detail, leads to a huge amount of CPU time beyond imagination.

## 5. Conclusions

An adaptive modeling and simulation have been introduced for the reliable CPU-time-efficient simulation using MSC/Dytran for large-scale complex fluid-structure interaction systems with two-phase flow and demonstrated through the illustrative numerical experiment with the pressurized LNG insulation containment. The critical time and the critical region of the FSI system were examined through the coarse-scale global rigid sloshing simulation, while the detailed hydroelastic response in the local region during the short time period starting from the critical time was obtained using the fine-scale full fluid-structure interaction model including the upper NG flow. The mapping of the global analysis results onto the fine-scale model was performed by the in-house program. It has been verified from the numerical experiment that the proposed method can successfully analyze the hydrodynamic response to the detailed component level which was not possible by the conventional standard FSI simulation technique owing to a huge amount of CPU time. Furthermore, it has been found that the upper NG flow provides the cushioning effect against the hydrodynamic impact of LNG by reducing the peak effective stress up to 10%.

## References

- Aquelet, N., Souli, M. and Olovsson, L. (2006), "Euler-Lagrange coupling with damping effects: Application to slamming problems", *Comput. Meth. Appl. Mech. Eng.*, **195**, 110-132.
- Barler, B., Humpherys, J., Lafitte, O., Rudd, Keith. and Zumburn, K. (2008), "Stability of isentropic Navier-Stokes shocks", *Appl. Math. Lett.*, **21**(7), 742-747.
- Cho, J.R. and Lee, S.Y. (2003), "Dynamic analysis of baffled fuel-storage tanks using the ALE finite element method", *Int. J. Numer. Meth. Fluids*, **41**(2), 185-208.
- Cho, J.R. and Song, J.M. (2001), "Assessment of classical numerical models for the separate liquid-structure analysis", *J. Sound Vib.*, **239**(5), 995-1012.
- Cho, J.R., Lee, H.W., Sohn, J.S., Kim, G.J. and Woo, J.S. (2006), "Numerical investigation of hydroplaning characteristics of three-dimensional patterned tire", *Eur. J. Mech. A-Solid*, **25**, 914-926.

- Cho, J.R., Song, J.M. and Lee, J.K. (2001), "Finite element techniques for the free-vibration and seismic analysis of liquid-storage tanks", *Finite Elem. Anal. D.*, **37**(6-7), 467-483.
- Farhat, C., Lesoinne, M. and Letallec, P. (1998), "Load and motion transfer algorithms for fluid/structure interaction problems with non-matching discrete interfaces: Momentum and energy conservation, optimal discretization and application to aeroelasticity", *Comput. Meth. Appl. Mech. Eng.*, **157**, 95-114.
- Housner, G.W. (1963), "The dynamic behavior of water tanks", *B. Seismol. Soc. Am.*, **53**, 381-387.
- Kyoung, J.H., Hong, S.Y., Kim, J.H. and Bai, K.J. (2005), "Finite-element computation of wave impact load due to a violent sloshing", *Ocean Eng.*, **32**, 2020-2039.
- Longatte, E., Verreman, V. and Souli, M. (2009), "Time marching for simulation of fluid-structure interaction problem", *J. Fluids Struct.*, **25**, 95-111.
- Mackerle, J. (1999), "Fluid-structure interaction problems, finite element and boundary element approaches a bibliography (1995-1998)", *Finite Elem. Anal. D.*, **31**, 231-240.
- Mao, K.M. and Sun, C.T. (1991), "A refined global-local finite element analysis method", *Int. J. Numer. Meth. Eng.*, **32**(1), 29-43.
- Morand, H.J.P. and Ohayon, R. (1995), *Fluid Structure Interaction: Applied Numerical Methods*, Wiley, New York.
- MSC/Dytran (2008), User's manual (version 4.5), The MacNeal Schwendler Corp., Los Angeles, CA, USA.
- Piperno, S., Farhat, C. and Larrouturou, B. (1995), "Partitioned procedure for the transient solution of coupled problems – Part I. Model problem, theory and two-dimensional application", *Comput. Meth. Appl. Mech. Eng.*, **124**(1-2), 79-112.
- Rajasankar, J., Iyer, N.R. and Appa Rao, T.V.S.R. (1993), "A new 3-D finite element model to evaluate added mass for analysis of fluid-structure interaction problems", *Int. J. Numer. Meth. Eng.*, **36**, 997-1012.
- Schäfer, M. and Teschauer, I. (2001), "Numerical simulation of coupled fluid-soil problems", *Comput. Meth. Appl. Mech. Eng.*, **190**, 3645-3667.
- Sigrist, J.F. and Abouri, D. (2006), "Numerical simulation of a non-linear coupled fluid-structure problem with implicit and explicit coupling procedure", *Proc. ASME Pressure Vessel and Piping Division Conference*, Vancouver, Canada.
- Xia, G.H., Zhao, Y. and Yeo, J.H. (2009), "Parallel unstructured multigrid simulation of 3D unsteady flows and fluid-structure interaction in mechanical heart valve using immersed membrane method", *Comput. Fluids*, **38**, 71-79.